REPORT DOCUMENTATION PAGE

Form Approved
OMB No. 0704-0188

1. REPORT DATE *(DD-MM-YYYY)*	**2. REPORT TYPE**	**3. DATES COVERED** *(From - To)*
06-04-2011	Technical Paper	MAR 2011 - APR 2011

4. TITLE AND SUBTITLE

Active Infrared Multispectral Imaging of Chemicals on Surfaces

5a. CONTRACT NUMBER
FA8720-05-C-0002

5b. GRANT NUMBER

5c. PROGRAM ELEMENT NUMBER

6. AUTHOR(S)

Anish K. Goyal, Melissa Spencer, Michael Kelly, Joseph Costa, Michael DiLiberto, Emily Meyer, and Thomas Jeys

5d. PROJECT NUMBER

5e. TASK NUMBER

5f. WORK UNIT NUMBER

7. PERFORMING ORGANIZATION NAME(S) AND ADDRESS(ES)

MIT Lincoln Laboratory
244 Wood Street
Lexington, MA 02420

8. PERFORMING ORGANIZATION REPORT NUMBER

9. SPONSORING / MONITORING AGENCY NAME(S) AND ADDRESS(ES)

AFLCMC/PZE
20 Schilling Circle, Bldg 1305
Hanscom AFB, MA 01731

10. SPONSOR/MONITOR'S ACRONYM(S)

AFLCMC/PZE

11. SPONSOR/MONITOR'S REPORT NUMBER(S)

12. DISTRIBUTION / AVAILABILITY STATEMENT

DISTRIBUTION STATEMENT A. Approved for public release; distribution is unlimited.

13. SUPPLEMENTARY NOTES

14. ABSTRACT

We investigated the signature phenomenology of long-wave infrared (LWIR) reflectance of contaminated surfaces using a quantum-cascade laser (QCL) that runes from n = 9.1 to 9.8 um and a HgCdTe focal-plane-array (FPA) with custom read-out integrated circuit (ROIC). A liquid chemical, diethyl phthalate (DEP), was applied to a variety of substrates such as diffusely reflecting gold, concrete, asphalt, and sand. Multispectral image-cubes of the scattered radiation were generated over 81 wavelengths in steps of 1 cm^-1 at standoff distances ranging from 0.1 to 5 meters. For idealized substrates such as diffusely reflecting gold, the experimentally measured signatures are in good agreement with theoretical calculations. Clear signatures were also obtained for contaminated concrete, asphalt, and sand. These measurements demonstrate the potential of this technique for detecting and classifying chemicals on native outdoor surfaces.

15. SUBJECT TERMS

chemical imaging, multispectral imaging, hyperspectral imaging, vibrational spectroscopy, infrared spectroscopy, quantum cascade lasers, HgCdTe, focal plane arrays

16. SECURITY CLASSIFICATION OF:			**17. LIMITATION OF ABSTRACT**	**18. NUMBER OF PAGES**	**19a. NAME OF RESPONSIBLE PERSON**
U					Zach Sweet
a. REPORT	**b. ABSTRACT**	**c. THIS PAGE**	SAR	11	**19b. TELEPHONE NUMBER** *(include area code)*
U	U	U			781-981-5997

Standard Form 298 (Rev. 8-98)
Prescribed by ANSI Std. Z39.18

MS-51262 revised

Active infrared multispectral imaging of chemicals on surfaces*

Anish K. Goyal, Melissa Spencer, Michael Kelly, Joseph Costa,
Michael DiLiberto, Emily Meyer, and Thomas Jeys

MIT Lincoln Laboratory, 244 Wood Street, Lexington, MA 02420-9108

ABSTRACT

We investigated the signature phenomenology of long-wave infrared (LWIR) reflectance of contaminated surfaces using a quantum-cascade laser (QCL) that tunes from $\lambda = 9.1$ to 9.8 μm and a HgCdTe focal-plane-array (FPA) with custom read-out integrated circuit (ROIC). A liquid chemical, diethyl phthalate (DEP), was applied to a variety of substrates such as diffusely reflecting gold, concrete, asphalt, and sand. Multispectral image-cubes of the scattered radiation were generated over 81 wavelengths in steps of 1 cm^{-1} at standoff distances ranging from 0.1 to 5 meters. For idealized substrates such as diffusely reflecting gold, the experimentally measured signatures are in good agreement with theoretical calculations. Clear signatures were also obtained for contaminated concrete, asphalt, and sand. These measurements demonstrate the potential of this technique for detecting and classifying chemicals on native outdoor surfaces.

Keywords: chemical imaging, multispectral imaging, hyperspectral imaging, vibrational spectroscopy, infrared spectroscopy, quantum cascade lasers, HgCdTe, focal plane arrays

1. INTRODUCTION

The detection and classification of chemicals on surfaces is of great importance for a variety of civilian and military applications. Very sensitive techniques, such as mass spectrometry, exist for surface sensing but these require a physical transfer of the chemicals from the surface into the instrument [1, 2]. It is, instead, highly desirable that detection and classification be achieved at standoff distances (>1 meter) with high areal-coverage-rates [3]. Of the demonstrated standoff techniques, the most promising ones are laser-induced breakdown spectroscopy (LIBS) [4, 5], Raman [6-8], and long-wave infrared (LWIR) spectroscopy [9]. As compared to Raman and LIBS, the LWIR techniques have the advantage of being potentially eye-safe at the target. Within LWIR spectroscopy, the methods can be divided into those that are passive [10-12] and those that utilize active illumination. The primary active techniques can further be classified according to whether they measure the optical reflectance [13-19] or a differential temperature change through the photothermal effect [20-23].

The work presented here is based upon actively illuminated LWIR reflectance spectroscopy. Recently, there has been particular interest in utilizing this technique for the standoff detection of explosives (see [24] and references therein). However, most of the work to date in this area has involved the detection of explosives on idealized substrates and under idealized configurations in order to achieve classification. These situations are unlikely to be encountered in the field. Recently, there have been efforts to detect explosives on substrates under conditions that can realistically be encountered [15, 22, 24]. The present work is an investigation of the signature phenomenology of liquid chemicals on realistic outdoor surfaces. Sensing is achieved using an imaging focal-plane-array (FPA) in combination with quantum-cascade-laser (QCL) illumination. To the best of our knowledge, this is the first demonstration of multispectral imaging of liquid chemicals on realistic outdoor surfaces using laser illumination.

* This work was sponsored by the Department of the United States Air Force under Air Force contract No. FA8721-05-C-0002. The opinions, interpretations, conclusions, and recommendations are those of the authors and are not necessarily endorsed by the United States Government.

2. EXPERIMENTAL SETUP

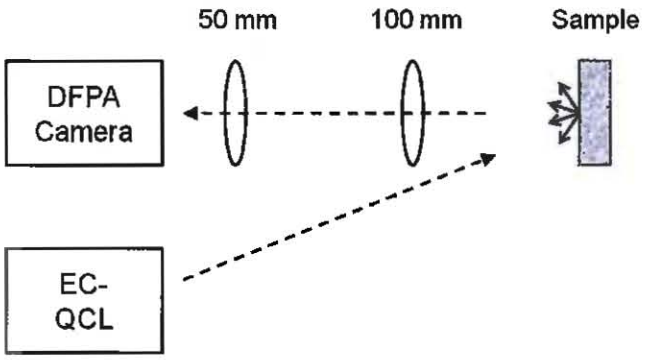

Figure 1: Experimental setup used for most of the measurements. The sample of interest is illuminated with an external-cavity QCL at an angle-of-incidence of ~30°. The scattered radiation is imaged at the digital focal-plane-array (DFPA) camera. The laser is stepped through 81 wavelengths spanning $\lambda = 9.1–9.8$ μm in steps of 1 cm^{-1} to generate an 81-frame multispectral image-cube.

2.1 Optical configuration

The experiments involve illuminating the sample of interest with a tunable QCL and capturing the scattered radiation using a LWIR camera. Figure 1 depicts the configuration for measurements at a standoff distance of 0.1 meter. An external-cavity QCL (EC-QCL) from Daylight Solutions [25] illuminates the sample at an angle-of-incidence (AOI) of ~30°. The sample surface is oriented to be approximately parallel to the FPA. An afocal telescope comprising anti-reflection-coated germanium lenses is used to image the scattered radiation at the FPA with an optical magnification of 2. The pixel size of the FPA is 30 μm resulting in a spatial resolution at the sample of 60 μm.

The EC-QCL is scanned from $\lambda = 9.1–9.8$ μm in steps of 1 cm^{-1} and an image is captured at each step to generate an 81-frame multispectral image-cube. The EC-QCL is operated in pulsed mode with a pulse length and repetition frequency of typically 500 ns and 10 kHz, respectively. The peak power from the QCL was normalized at each wavelength such that the response at the camera was spectrally flat when the sample was a diffuse-reflection standard [26]. The peak laser power at each wavelength was about 50 mW.

The camera is based on unique digital-pixel FPA (DFPA) technology [27, 28]. The DFPA used for these measurements utilizes a 256 x 256 HgCdTe detector array that is bump-bonded to a custom read-out integrated-circuit (ROIC). Unlike conventional analog FPAs, the DFPA incorporates an analog-to-digital converter (ADC) underneath each pixel. The ADC of the DFPA operates by counting the number of times a small capacitor is charged by the HgCdTe photodiode current. Every time the capacitor's voltage exceeds a set point, an associated comparator is triggered causing the capacitor to discharge and the event to be recorded by an up/down counter. This counter can be dynamically enabled or disabled. Furthermore, the counter can be dynamically configured to either add or subtract counts. At the end of an acquisition period, the digital values associated with the counter are read-out through fast digital shift-register operations.

The DFPA architecture enables a suite of unique capabilities that are relevant for active LWIR multispectral imaging systems. In particular, two capabilities of the DFPA are especially relevant for the measurements presented here because they suppress the passive thermal background. First, the DFPA can time-gate the response with sub-microsecond resolution by enabling the counter only while the laser is illuminating the scene. Between pulses, counting does not have to be enabled and therefore the intra-pulse passive thermal background does not contribute to the signal. The DFPA can be programmed to add an arbitrary number of pulses. For the measurements presented here, the signals were typically integrated over 30 pulses. The second important capability is called passive background subtraction. In the LWIR around $\lambda = 10$ μm, the blackbody radiation contribution to the signal can be larger than the active signal of interest. Therefore, it is critical to subtract this passive thermal background. Rather than performing this background subtraction off-chip at the computer by comparing two images, the DFPA can perform background subtraction on-chip.

This is accomplished simply by the counting down between laser pulses for a time equal to the count-up time while the laser was on. In this way, the resulting counter value represents only the active signal of interest. Combining time-gating with background subtraction significantly reduces the deleterious effects of the passive thermal background.

2.2 Chemical simulant and substrates

The liquid chemical chosen for this work is diethyl phthalate (DEP). DEP is safe to handle and has similar surface tension and viscosity to VX [29]. Figure 2 plots the absorption spectrum of DEP. Two absorption peaks that overlap the tuning range of the EC-QCL are $\lambda = 9.32$ μm and 9.61 μm. The complex refractive index of DEP was derived from the absorption spectrum using the Kramers-Kronig relation assuming a high-frequency refractive index of 1.50 [30].

The DEP was applied to a range of substrates. The idealized substrates were diffusely reflecting gold. These were made from glass slides that were roughened using grit and then sputter-coated with Ti/Au. For the surfaces that are representative of outdoor materials, standardized materials were not available. The concrete pavers were obtained from the hardware store, weathered asphalt pieces were found by the roadside, and sand was collected from the parking lot.

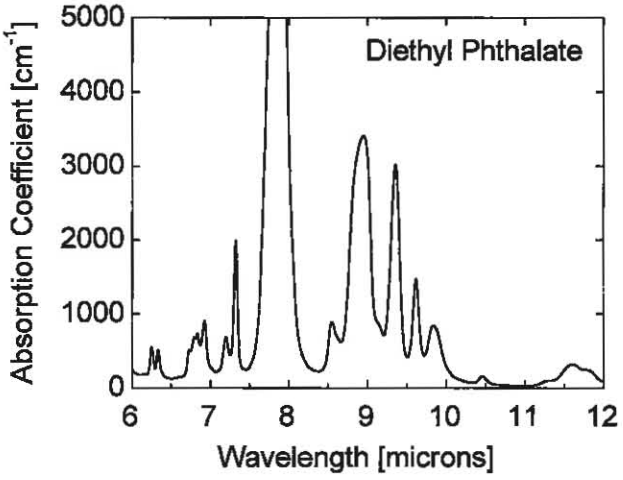

Figure 2: Absorption coefficient of diethyl phthalate (DEP).

3. THEORETICAL REFLECTANCE

Reflectance from native outdoor surfaces that are contaminated with liquid chemicals is a complex phenomenon that includes contributions from both the first-surface reflection at the chemical-air interface and the double-pass absorption within the film. The combination of these processes is sometimes called transflection.

The component that corresponds to double-pass absorption is illustrated by the case of a thin-film on a diffusely reflecting substrate. Referring to the schematic of the thin-film in Figure 3, a fraction of the illuminating radiation is reflected at the chemical/air interface and this light is not collected by the receiver. The light that is transmitted into the film is diffusely reflected by the substrate prior to being collected by the receiver. The measured reflectance spectrum can be written as

$$R_{abs} = F \cdot R_{sub}(\lambda) \cdot \exp\left[-\frac{4\pi}{\lambda}\kappa \cdot 2t\right] \tag{1}$$

where F is related to the collection efficiency of the receiver, R_{sub} is the reflectance at the chemical/substrate interface, λ is the free-space wavelength, κ is the imaginary part of the refractive index, and $2t$ is the double-pass path of the light within the chemical film. This is plotted in Figure 3 for a 10-μm-thick film of DEP taking $F \cdot R_{sub} = 5\%$. As expected, the reflectance minima are centered at the absorption peaks.

For a thick droplet, the light that is transmitted into the chemical is, to good approximation, fully absorbed. Only that light which is reflected at the chemical/air interface and is directed towards the receiver will be collected. This first-surface reflectance is given by (at normal incidence)

$$R_{refl} = G \cdot \frac{(n-1)^2 - \kappa^2}{(n-1)^2 + \kappa^2} \tag{2}$$

where G is related to the collection efficiency of the receiver and n is the real part of the refractive index. Since the real and imaginary parts of the index are related by the Kramers-Kronig relationship, each strong absorption feature corresponds to a region of anomalous dispersion in which the reflectance increases with increasing wavelength. This is clearly seen for each of the absorption features in Figure 3. As a result, the minima in the first-surface reflection spectra are shifted to shorter wavelengths as compared to the absorption features. The shift is larger for broader absorption peaks. For the two absorption peaks that are relevant for this work (λ = 9.32 μm and 9.61 μm), the reflection minima are shifted to λ = 9.26 μm and 9.58 μm which correspond to a shift of $\Delta\lambda$ = 0.06 μm and 0.03 μm, respectively. This point is relevant for the measurement results that are discussed in the next section.

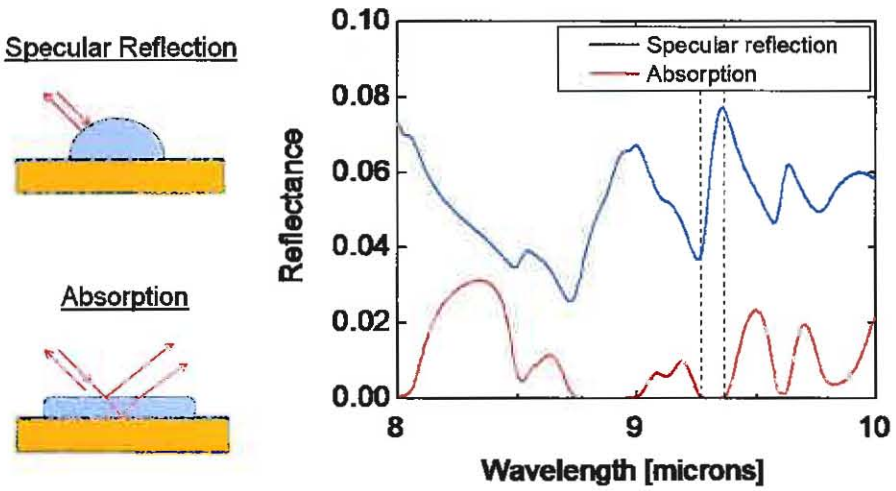

Figure 3: Illustration of two components of transflection: specular reflection at the chemical-air interface and absorption within the chemical. The plot shows the calculated specular reflection and absorption components for DEP.

For chemicals on diffusely reflecting outdoor surfaces, the transflection physics that leads to the measured reflectance spectrum can be complex. The reflectance spectrum depends upon factors such as the thickness of the chemical on the surface and the morphology of the surface. These, in turn, depend upon the details of the surface roughness and porosity, chemical viscosity, and interfacial surface tension. For a non-porous substrate where the chemical layer is likely to be thick, it is expected that the first-surface reflectance component will dominate. For a thin layer on a porous substrate, the absorption spectrum is expected to dominate. In reality, a combination of these two effects will play a role.

4. MEASUREMENTS AT CLOSE RANGE

A variety of samples were measured at a range of 0.1 meters using the experimental setup shown in Figure 1. These included idealized diffusely reflecting gold substrates and surfaces that are representative of native outdoor surfaces.

4.1 Diffusely reflecting gold substrate

To mimic the idealized cases described in the previous section, thin films and thick droplets of DEP were deposited on a diffusely reflecting gold substrate using a micro-pipetter. Figure 4 depicts the sample in both visible and infrared images. A row of 3 droplets (each 1 μL) was dispensed on the top row and fourth 10-μL droplet was dispensed on the

bottom row. The bottom row also includes a thin film in which a 1-μL droplet was spread using a cotton swab. The infrared image at $\lambda = 9.8$ μm represents a single frame (256 x 256 pixels) of an 81-frame multispectral image-cube. The laser illumination can be seen to have a higher intensity in the center of the scene. For the thin film, the rectangular region represents the area over which the pixel values are averaged. The reflectance that is derived from the multispectral image-cube is plotted versus wavelength as the colored, solid line. The measurement is in good agreement with the theoretical reflectance which assumes a uniform film thickness of 8 μm. For each of the droplets, one can clearly see a small region that corresponds to the first-surface reflection. The spectral reflectance derived from each of the four droplets was found to track the theoretical curve. For clarity, only the two curves that correspond most closely to the theoretical curve are plotted. These are found to match the theoretical curve to within 10%. This data demonstrates the ability to measure the both the first-surface reflection and absorption spectra of DEP within a single multispectral image-cube.

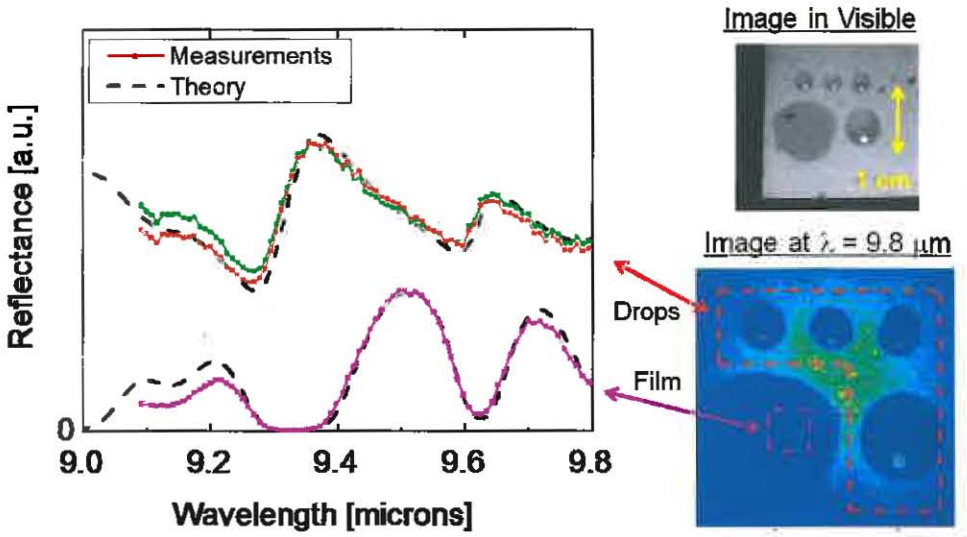

Figure 4: Measurement of droplets and thin film of DEP on a diffusely reflecting gold substrate. Both the first-surface reflection spectra from each of the 4 droplets and the absorption spectrum through the thin-film are observed in a single 81-frame multispectral image-cube. For clarity, only the two best first-surface reflection spectra are plotted.

4.2 Realistic outdoor substrates

The reflectance of clean and contaminated concrete pavers was measured. Figure 5 shows uncalibrated measurements of the reflectance from clean concrete, concrete that is wet with water, and concrete with a thin layer of DEP. As stated earlier, the concrete was oriented to be roughly parallel with the FPA (normal to the optical axis of the receiver) and the laser illumination AOI ~ 30°. The reflectance of clean concrete has a local maximum at $\lambda \sim 9.3$ μm. After applying water, the shape of the reflectivity spectrum does not change much presumably because the layer of water is very thin. For the sample with DEP, reflectance minima occur at about 9.3 μm and 9.6 μm as would be expected. This demonstrates the ability to discriminate between DEP and water contamination on concrete.

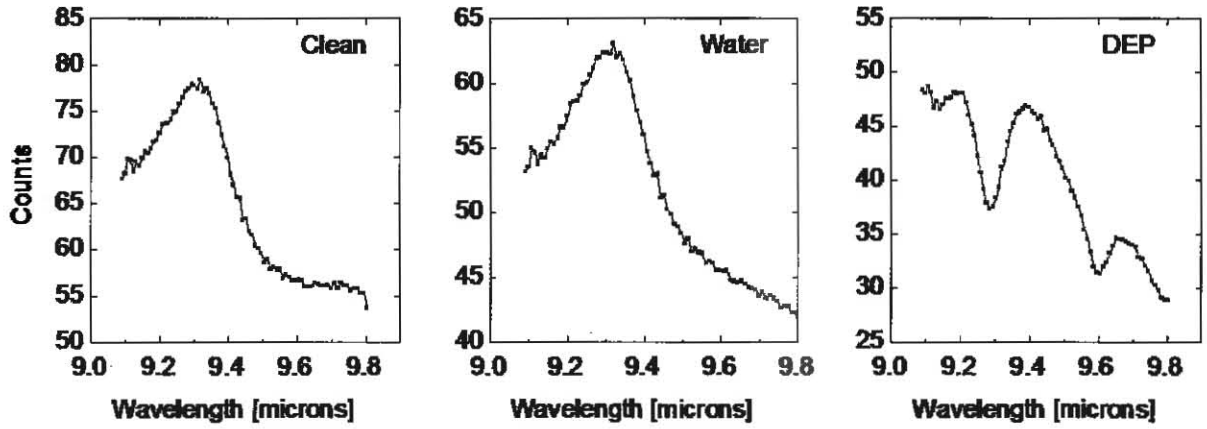

Figure 5: Spectral reflectance from clean concrete pavers (left), concrete with water (center), and concrete with DEP (right).

Calibrated reflectance measurements were made using controlled amounts of DEP. Figure 6 shows visible images of concrete pavers that are contaminated with DEP droplet volumes of 2-, 10-, and 20-μL. The DEP is readily absorbed into the concrete and spreads laterally to form a contaminated region that ranges in extent from ~0.5 cm to several cm. Multispectral images were acquired for each of these cases. The photograph on the right of Figure 6 indicates the field of view of the DFPA for the measurements and also the region over which the reflectance spectrum was averaged for the case of a 10-μL droplet.

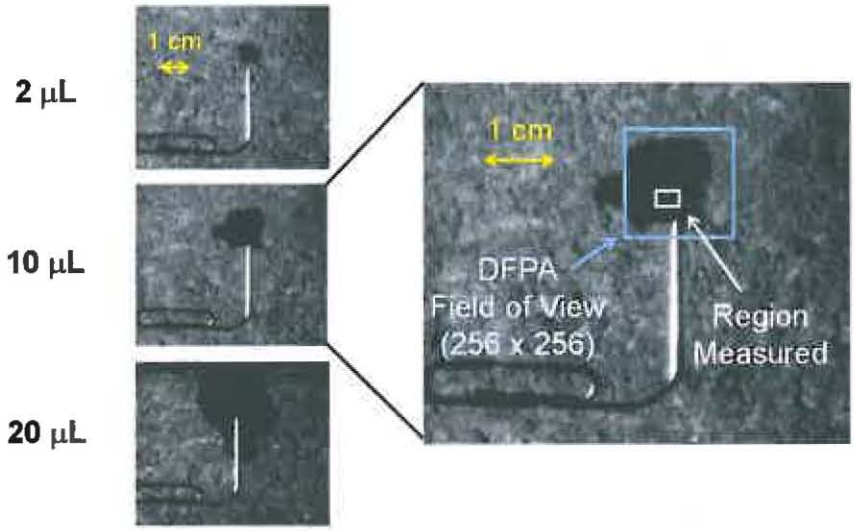

Figure 6: Visible photographs that show the contamination footprint of DEP on concrete pavers for several deposition volumes (left). The photograph on the right corresponds to a 10-μL droplet and indicates the field-of-view of the DFPA and the region over which the spectral reflectance was averaged.

The multispectral image-cubes were generated before and after chemical deposition. The graph on the left of Figure 7 plots the reflectance as a function of wavelength for the case of a 10-μL drop on concrete. The reflectance values are normalized to that of a diffusely reflecting gold standard [26]. The reflectance of clean concrete varies from about 5–9% and has a local maximum at $\lambda \approx 9.35$ μm. After application of DEP, the reflectance decreases and features that correspond to DEP can be seen. Taking the ratio of the contaminated-to-clean reflectance, one obtains the reflectance ratios that are plotted in the graph on the right. Note that the reflectance ratio is smoother than the raw reflectance data because systematic errors in the laser power normalization are cancelled by taking a ratio. For the 2-μL droplet, the

reflectance ratio exhibits a spectral feature with a modulation depth of about 5%. The minima are centered at 9.32 μm and 9.62 μm which are very close to the absorption peaks in DEP. As the droplet volume increases, the depth of the signature increases to more than 40% for the 20-μL droplet. Note also that the minima in the reflectance ratio shifts to the shorter wavelengths of 9.28 μm and 9.60 μm. This indicates that the reflectance signature is transitioning from one that probes the absorption in the thin film to one that is dominated by the first-surface reflection. This data shows that, because of the complexity of the signature, account needs to be taken of the various transflection processes. Other groups have arrived at similar conclusions when detecting trace explosives [24].

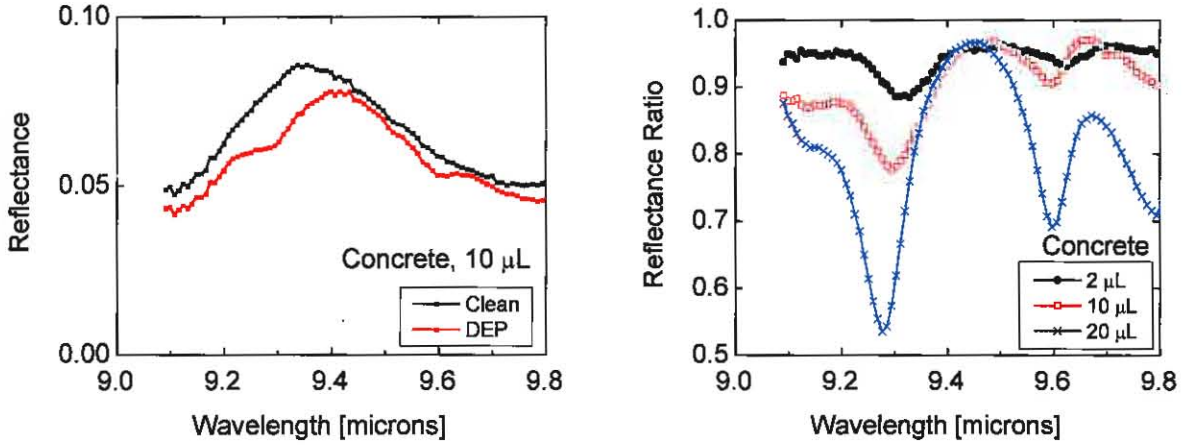

Figure 7: Reflectance (left) and reflectance ratio (right) for clean and DEP-contaminated concrete.

Measurements on asphalt are shown in Figure 8. Asphalt is a coarse composite of minerals and bitumen. It is expected that the reflectance will vary with position. However, for these measurements no effort was made to probe a particular component of asphalt or to understand how the reflectance varies with position. The graph on the left of Figure 8 plots the reflectivity of clean asphalt which is found to vary between 7–12% relative to a gold reflectance standard. Spectral features that are clearly attributable to DEP are observed in the raw reflectance data for the 10-μL volume. Taking the reflectance ratio, one find that strong features are obtained for all deposition volumes. This can be attributed to the fact that the chemical is not absorbed as readily into the asphalt as compared to concrete. The modulation in the reflectance ratio is >30%. The minima occur at 9.28 μm and 9.60 μm and indicate that the first-surface reflection dominates the spectra. This is consistent with the relatively non-porous nature of asphalt.

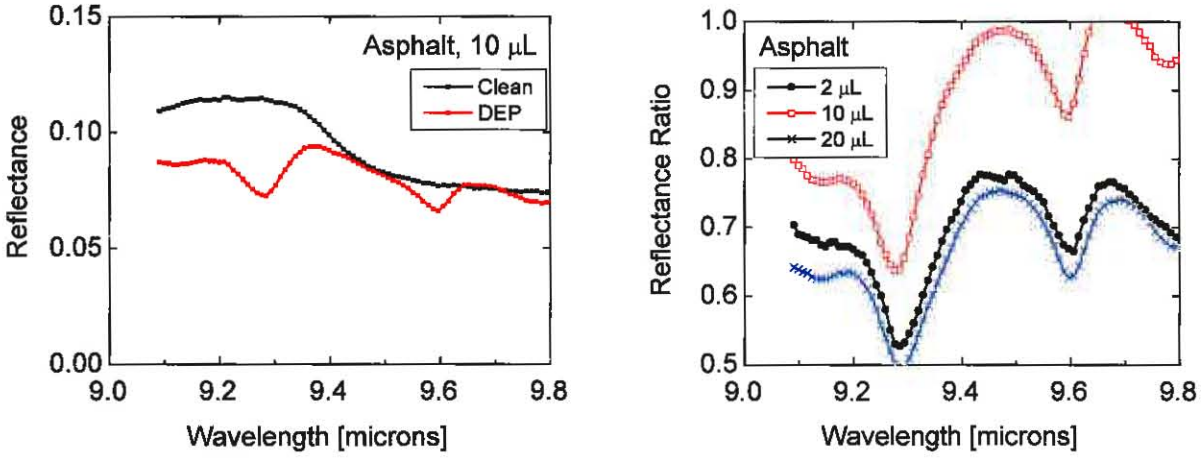

Figure 8: Reflectance (left) and reflectance ratio (right) for clean and DEP-contaminated asphalt.

Finally, DEP was applied to sand and the data are shown in Figure 9. The plot on the left shows the raw reflectance of clean and contaminated sand. The reflectance of clean sand varies from about 10–20% over this wavelength band. Upon application of DEP, the reflectance decreases. The reflectance ratio is shown for only the 10- and 20-μL volumes. We were not able to locate the 2-μL drops in the scene. Signatures are observed for both of the larger drop volumes with modulation depths of about 15% and 20% for 10- and 20-μL drops, respectively. These modulation depths are less than for the cases of concrete and asphalt, but are still clearly measurable. This result is not surprising given the highly porous nature of sand. The minima in the reflectance ratios are centered at 9.32 μm and 9.62 μm which indicate probing of the absorption within the chemical. This is the expected result based on Kubelka-Munk theory which is relevant for diffuse reflectance within powdered samples [31].

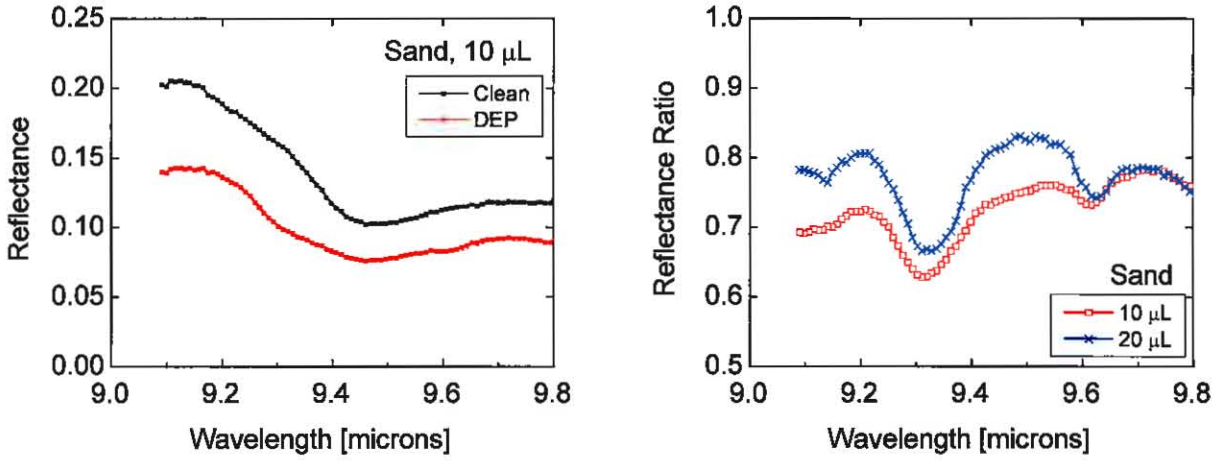

Figure 9: Reflectance (left) and reflectance ratio (right) for clean and DEP-contaminated sand.

5. MEASUREMENTS AT LONGER RANGE

Preliminary reflectance measurements of contaminated surfaces were performed at standoff distances of 1 and 5 meters. For these measurements, the afocal telescope was replaced with a LWIR camera lens (50 mm, f/1.4). Moderate, yet uncontrolled, amounts of DEP were applied to the substrates. Unless otherwise specified, measurements were performed as outlined in Section 2.

Figure 10 plots the measured reflectance of DEP-contaminated concrete pavers at a range of 1 meter for which the laser AOI ~ 5°. At normal incidence, spectral features attributable to DEP are observed with a modulation of ~20%. When tilting the paver by 45°, such that the laser-beam polarization is in the plane of incidence, the spectral features remain visible with a modulation depth of ~15%. The magnitude of the reflectance is found to decrease by almost a factor of 2. For both 0° and 45°, the signatures are dominated by first-surface specular reflection. The fact that a significant reflectance is observed for a tilt angle of 45° indicates that the chemical conformally coats the concrete to some extent and that microfacets are responsible for a portion of the specular reflection being collected by the receiver.

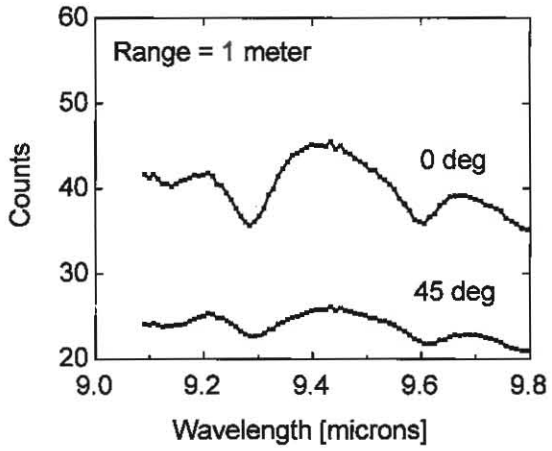

Figure 10: Reflectance at range of 1 meter for DEP on concrete at both 0° (normal to FPA) and 45°.

Reflectance measurements were made at a range of 5 meters for samples of DEP-coated diffused gold. At this range, the illumination AOI ~ 1°. The beam size at the sample was such that only about 100 pixels were illuminated. The angle of the sample could be adjusted to enhance the specular reflection back to the camera. In this case (see left side of Figure 11), the reflectance signal was large and follows closely the theoretical curve (compare with Figure 4). When the sample was misoriented to allow only the diffusely scattered radiation to reach the receiver, the signal decreases significantly and the spectral features are due to absorption in the film (right side of Figure 11).

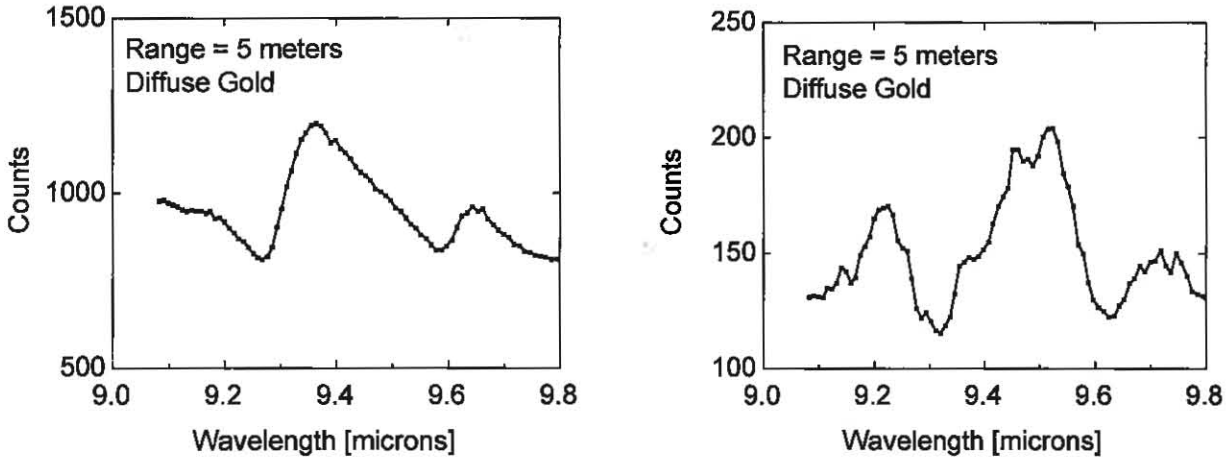

Figure 11. Reflectance of DEP on diffuse gold at 5-meter range. The sample was aligned for either direct specular reflection (left) or misaligned for diffuse reflection (right).

6. SUMMARY

In summary, we have demonstrated that strong LWIR reflectance signatures exist for liquid chemicals on native outdoor surfaces. We also demonstrate the utility of an active LWIR multispectral imaging system that is based on the combination of a QCL illuminator and DFPA camera. Liquid chemicals were detected at standoff distances of up to 5 meters.

REFERENCES

[1] Venter, A., Nefliu, M., Cooks, R. G., "Ambient desorption ionization mass spectrometry," Trends Anal. Chem. 27, 284-290 (2008).

[2] Seto, Y., Kanamori-Kataoka, M., Tsuge, K., *et al.*, "Sensing technology for chemical-warfare agents and its evaluation using authentic agents," Sensors and Actuators B: Chemical 108, 193-197 (2005).

[3] Fountain III, A. W., Christesen, S. D., Guicheteau, J. A., Pearman, W. F., and Chyba, T., "Long range standoff detection of chemical and explosive hazards on surfaces," Proc. SPIE 7484, 748403-11 (2009).

[4] Gottfried, J., De Lucia, F., Munson, C., and Miziolek, A., "Laser-induced breakdown spectroscopy for detection of explosives residues: a review of recent advances, challenges, and future prospects," Anal. Bioanal. Chem. 395, 283-300 (2009).

[5] Ford, A., Waterbury, R. Rose, J., *et al.*, "Extension of standoff explosives detection systems to CBRN threats," Proc. SPIE 7665, 76650Y-10 (2010).

[6] Wu, M., Ray, M., Fung, K. H., Ruckman, M. W., Harder, D., and Sedlacek III, A., J., "Stand-off detection of chemicals by UV Raman spectroscopy," Appl. Spectroscopy 54, 800-806 (2000).

[7] Ponsardin, P., Higdon, S., Chyba, T., and Armstrong, W., "Expanding applications for surface-contaminants sensing using the laser interrogation of surface agents (LISA) technique," Proc. SPIE 5268, 321-327 (2004).

[8] Christesen, S. D., Lochner, J. M., Hyre, A. M., Emge, D. K., and Jones, J. P., "UV Raman spectra and cross sections of chemical agents," Proc. SPIE 6218, 621809-8 (2006).

[9] Sharpe, S., Johnson, T., Sams, R., *et al.*, "Infrared spectral signatures: Creation of reference data for vapors and liquids," Intl. J. High-Speed Electronics and Systems 18, 231-250 (2008).

[10] Theriault, J. M., Hancock, J., Jensen, J. O., and Puckrin, E., "Passive standoff detection of liquid surface contaminants: Recent results with CATSI," Proc. SPIE 5268, 310-320 (2004).

[11] Farley, V., Vallieres, A., Villemaire, A., *et al.*, "Chemical agent detection and identification with a hyperspectral imaging infrared sensor," Proc. SPIE 6739, 673918-12 (2007).

[12] Gittins, C. M., and Marinelli, W. J., "AIRIS multispectral imaging chemical sensor," Proc. SPIE 3383, 65 (1998).

[13] Samuels, A. C., Zhu, C., Williams, B. R., et al., "Improving the linearity of infrared diffuse reflectance spectroscopy data for quantitative analysis," Anal. Chem. 78, 408-415 (2005).

[14] Bell, A. Dyer, C., Jones, A. W., and Kinnear, K., "Standoff liquid CW detection," Proc. SPIE 5268, 302-309 (2004).

[15] Harig, R., Braun, R., Dyer, C., Howle, C., and Truscott, B., "Short-range remote detection of liquid surface contamination by active imaging Fourier transform spectrometry," Opt. Express 16, 5708-5714 (2008).

[16] Van Neste, C. W., Senesac, L. R., and Thundat, T., "Standoff photoacoustic spectroscopy," Appl. Phys. Lett. 92, 234102-3 (2008).

[17] Hinkov, B., Fuchs, F., Kaster, J. M., et al., "Broad band tunable quantum cascade lasers for stand-off detection of explosives," Proc. SPIE 7484, 748406-13 (2009).

[18] Phillips M. C., and Ho, N., "Infrared hyperspectral imaging using a broadly tunable external cavity quantum cascade laser and microbolometer focal plane array," Opt. Express 16, 1836-1845 (2008).

[19] Bernacki, B. E., and Phillips, M. C., "Standoff hyperspectral imaging of explosives residues using broadly tunable external cavity quantum cascade laser illumination," Proc. SPIE 7665, 76650I-10 (2010).

[20] Furstenberg, R., Kendziora, C. A., Stepnowski, J., Stepnowski, S. V., et al., "Stand-off detection of trace explosives via resonant infrared photothermal imaging," Appl. Phys. Lett. 93, 224103-3 (2008).

[21] Kendziora, C. A., Furstenberg, R., Papantonakis, M., et al., "Advances in standoff detection of trace explosives by infrared photo-thermal imaging," Proc. SPIE 7664, 76641J-12 (2010).

[22] Mukherjee, A., Von der Porten, S., and Patel, C. K. N., "Standoff detection of explosives substances at distances of up to 150 m," Appl. Opt. 49, 2072-2078 (2010).

[23] Skvortsov, L. A., and Maksimov, E. M., "Application of laser photothermal spectroscopy for standoff detection of trace explosive residues on surfaces," Quant. Electronics 40, 565-578 (2010).

[24] Fuchs, F., Hugger, S., Kinzer, M., et al., "Imaging standoff detection of explosives using widely tunable midinfrared quantum cascade lasers," Opt. Engr. 49, 111127 (2010).

[25] Daylight Solutions, Inc. (San Diego, CA), www.daylightsolutions.com.

[26] Infragold reflectance target, Labsphere, Inc. (North Sutton, NH), www.labsphere.com.

[27] Kelly, M., Berger, R., Colonero, C., et al., "Design and testing of an all-digital readout integrated circuit for infrared focal plane arrays," Proc. SPIE 5902, 59020J-11 (2005).

[28] Tyrrell, B., Berger, R., Colonero, C., et al., "Design approaches for digitally dominated active pixel sensors: Leveraging Moore's law scaling in focal plane readout design," Proc. SPIE 6900, 69000W (2008).

[29] Bartelt-Hunt, S. L., Knappe, D. R. U., and Barlaz, M. A., "A review of chemical warfare agent simulants for the study of environmental behavior," Crit. Rev. Environmental Sci. & Techn. 38, 112-136 (2008).

[30] Ohta, K., and Ishida, H., "Comparison among several numerical integration methods for Kramers-Kronig Transformation," Appl. Spectroscopy 42, 952-957 (1988).

[31] Fuller, M. P., and Griffiths, P. R., "Diffuse reflectance measurements by infrared Fourier transform spectrometry," Anal. Chem. 50, 1906-1910 (1978).